Acta Materialia 202 (2021) 124–134

Contents lists available at ScienceDirect

Acta Materialia

journal homepage: www.elsevier.com/locate/actamat

Bimodality of incipient plastic strength in face-centered cubic high-entropy alloys

Yakai Zhao[a], Jeong-Min Park[b], Jae-il Jang[b,*], Upadrasta Ramamurty[a,c,1,*]

[a] School of Mechanical and Aerospace Engineering, Nanyang Technological University, Singapore 639798
[b] Division of Materials Science and Engineering, Hanyang University, Seoul 04763, Republic of Korea
[c] Institute of Materials Research and Engineering, Agency for Science, Technology and Research (A*STAR), Singapore 138634

ARTICLE INFO

Article history:
Received 11 September 2020
Revised 26 October 2020
Accepted 26 October 2020
Available online 29 October 2020

Keywords:
High-entropy alloy
nanoindentation
pop-in
statistical analysis
short-range ordering

ABSTRACT

Spherical tip nanoindentation experiments on two typical face-centered cubic high-entropy alloys (HEAs), CoCrFeNi and CoCrFeMnNi in as-solutionized and aged conditions were performed using tips of two different radii. Large datasets of the strength at the first pop-in were obtained and their statistical nature were analyzed to gain insights into the micromechanisms responsible for the onset of incipient plasticity in HEAs that are notionally monophasic. In all the cases examined, the probability density distributions were bimodal in nature. The deconvoluted distributions were utilized to estimate the activation volumes of the underlying deformation mechanisms. They show that when the probed material's volume is relatively small, heterogeneous dislocation nucleation aided by monovacancies occurs at lower indentation stresses; this followed by homogeneous dislocation nucleation at high loads, resulting in strengths corresponding to the theoretical strengths. When a substantially larger volume is sampled, by using a larger radius tip, either the preexisting dislocation mediated ones at low stresses or vacancy cluster /grain boundary aided heterogeneous dislocations nucleation at higher stresses become dominant. Increasing the chemical short-range order in the alloy via high temperature aging leads to overall strengthening of the alloy by enhancing stress required for the homogeneous dislocation nucleation. Implications of such plurality of mechanisms with overlapping strength distributions at HEA's disposal in imparting high strength-ductility combinations are discussed.

1. Introduction

The distinct facet of a high-entropy alloy (HEA) is that it is monophasic–as far as most conventional microscopy and X-ray diffraction (XRD) techniques can detect–in spite of the fact that the alloy is made of at least three or more elements in (near-)equimolar concentrations so as to maximize the configurational disorder. The first such alloy to be reported is the face-centered cubic (fcc) CoCrFeMnNi [1], which led to active research focusing on the 3d transition metal based fcc HEA families [2–5]. Recently, however, consensus is emerging that these are not ideal solid solutions at the atomic length scales, but some level of chemical clustering and/or short-range ordering occurs at nm length scales. Indeed, a wide and spatially varied distribution in the local stacking fault energies (SFEs) has been reported in fcc HEAs [6–8], implying that HEAs are chemically inhomogeneous, since SFEs are sensitive to the local atomic configuration. Such nanometer scale heterogeneity has been verified through both detailed microscopy [9–11] and simulations [8,12,13]. The presence of any short range ordered (SRO) domains in the microstructure can increase the activation energy barrier for dislocation mediated plasticity [14], which, in turn, will enhance the work hardening and strain-rate sensitivity of HEAs [5,15]. This is possibly the fundamental reason for some unique combination of mechanical properties of HEAs.

The present work is initiated with the following premise: *if indeed the HEAs are compositionally inhomogeneous at the nanometric scales, which are comparable to the length scales associated for the sources of unit deformation mechanisms, it is possible that incipient plasticity, which depends directly on the nature and activation of the local defect, also varies spatially.* This could manifest, possibly, in a strength distribution that is distinct from those seen in conventional metals and alloys, provided that the spatial resolution of the probe used for measuring the strength corresponds to the characteristic microstructural length scale. For examining this possibility, the spherical tip nanoindentation technique, through which

* Corresponding authors.
E-mail addresses: jijang@hanyang.ac.kr (J.-i. Jang), uram@ntu.edu.sg (U. Ramamurty).

[1] Upadrasta Ramamurty was an Editor of the journal during the review period of the article. To avoid a conflict of interest, Upadrasta Ramamurty was blinded to the record and another editor processed this manuscript.

https://doi.org/10.1016/j.actamat.2020.10.066
1359-6454/

the elastic-to-elastoplastic transition can be precisely captured by measuring the load, P_I, at the first discrete displacement burst (or 'pop-in') on the load–displacement (P–h) curve [16–18], is ideally suited. Since the deformed volume is usually very small (a few nm^3), especially when a tip with a small radius (about a micron or less) is used, the first pop-in is often attributed to the nucleation of dislocations in crystals underneath the indenter [17,18]. Since the first pop-in is a measure of the onset of plastic deformation at the micro-scale, insights into the nature of the incipient plasticity can be gained through a detailed analysis of the statistics of the strength associated with P_I [17–20]. Indeed, such an approach was widely utilized to reveal fundamental aspects of plastic deformation such as quantifying the activation volume and energy for dislocation nucleation [21–23].

In the context of HEAs, Zhu et al. [24] performed spherical nanoindentation experiments at various temperatures on the CoCrFeMnNi HEA to obtain the activation volume and energy. On that basis, they concluded that the vacancy-mediated heterogeneous dislocation nucleation mechanism controls plasticity in that HEA. Similarly, Mridha et al. [25] examined several fcc HEAs and reported thermal activation parameters and suggested that heterogeneous dislocation nucleation from defects such as surface ledges, surface defects, vacancy clusters and/or impurity atoms is responsible for the incipient plasticity.

Most of the aforementioned analyses, including all those reported hitherto on HEAs, assume unimodal strength distribution. This, in turn, assumes implicitly that the measured distributions are solely due to the operation of a solitary deformation mechanism [22,23,26]. Although the possibility of simultaneous operation of more than one deformation mechanism during spherical indentation on crystalline metals has not yet been examined, bimodal distributions in first pop-in strengths have been reported for metallic glasses (MGs). Perepezko et al. [27], who analyzed the statistics of incipient strengths obtained on four different MGs, asserted that the observed bimodality is a consequence of two distinct defect sites getting activated to form an incipient shear band. Nag et al. [20], who critically examined a large number of datasets, which were obtained on different MGs with various combinations of tip radius, loading rate, and structural state of the glass, show that the bimodality is significant only when a large radius tip and high loading rate combination is used.

An examination of the cumulative distributions of P_I reported on HEAs indicate to the possibility that they might also be bimodal (see, for example, the presence of a small shoulder in the distribution of strengths obtained with a loading rate of 2500 μN/s in [24] and on CoCrFeMnNi in [25]). To examine this possible bimodality in greater detail and to gain insights into the possible influence of SRO on the incipient plasticity, we conducted nanoindentation experiments on two widely-studied fcc HEAs, namely CoCrFeNi and CoCrFeMnNi, in the as-homogenized and aged conditions; the latter was utilized to examine if a higher fraction of SRO domains, which are possibly induced during the aging followed by slow cooling. Recently, Zhang et al. [11] have shown that such a heat treatment promotes the SRO formation in a CoCrNi medium-entropy alloy (MEA). We therefore followed the similar processing routes and examined the effects of aging on the strength statistics. For each condition, close 200 data points were generated and analyzed, so that the bimodal nature, if any, is robustly picked up.

2. Materials and experiments

Two fcc HEAs, with the nominal compositions (at.%) of $Co_{25}Cr_{25}Fe_{25}Ni_{25}$ and $Co_{20}Cr_{20}Fe_{20}Mn_{20}Ni_{20}$, are examined in this work. Ingots of them were synthesized by vacuum induction melting of pure metals. They were then hot-rolled, homogenized (at 1000 and 1100°C, respectively, for CoCrFeNi and CoCrFeMnNi) for 1 h, and water-quenched to obtain 'as-homogenized (AH)' samples. Some of the specimens were further aged at 900°C for 24 h, followed by slow furnace cooling. These are referred to as 'Aged' samples hereafter. All the specimens were mechanically polished first with sand papers (grit number up to 2000) and then electropolished (65 V, 30 s, and 15°C) in a mixture of 90% acetic and 10% perchloric acids, so as to remove any work hardened surface layer that may affect the pop-in results [28,29].

X-ray diffraction (XRD; Empyrean, Malvern Panalytical Ltd., Malvern, UK) and backscattered electron (BSE) imaging using scanning electron microscopy (SEM; Verios G4 XHR, Thermo Fisher Scientific, Hillsboro, OR, USA) were utilized for the structural characterization of the AH and Aged HEA samples. Nanoindentation tests were performed using the Nanoindenter-XP instrument (formerly MTS; now KLA Corporation, Milpitas, CA, USA) with two different spherical indenter tips with radii, R_i = 0.5 and 12.7 μm. Prior to each test, each tip's radius was calibrated using the Hertzian analysis [30] of the indentation data obtained on a reference fused quartz sample. All the tests were conducted with a fixed loading rate of 0.5 mN/s, and peak loads, P_{max} of 10 and 30 mN (for R_i = 0.5 and 12.7 μm, respectively). In order to generate statistically significant datasets, more than 200 tests were conducted on each material, using grid indentations with 25 μm as the horizontal and vertical spacing between successive indents. After the tests, we were able to collect ~166–197 data points that clearly show pop-ins from each condition. Since the HEA examined is polycrystalline, the indents fall on several grains that are oriented differently from each other. However, the crystal orientation effect is considered weak in the CoCrFeMnNi HEA [24], and hence, were neglected. Mapping of the results obtained also does not show any spatial correlation; see Fig. S1 in supplementary information (SI).

3. Results

3.1. Microstructures

The XRD scans obtained on the CoCrFeNi and CoCrFeMnNi samples in both AH and Aged states, displayed in Fig. 1, show identical peak positions, all of which correspond to a single fcc phase. This confirms that the aging process does not lead to formation of a new and distinct microstructural phase and the HEA remains monophasic. The lattice parameters, a, of CoCrFeNi and CoCrFeMnNi samples were estimated to be ~3.57 and ~3.59 Å, respectively, which correspond well with the literature values [31,32] and do not show significant change after the aging treatment. The microstructures of both the samples, displayed in Fig. 1, confirm that they consist of equiaxed grains with a few annealing twins; the average grain sizes, d, in AH CoCrFeNi and CoCrFeMnNi were found to be ~29 ± 11 and ~63 ± 25 μm, respectively. Upon aging, no significant change in d was noted, suggesting that the aging treatment did not coarsen the grains.

3.2. Strength distributions

Representative P–h responses measured on the CoCrFeNi and CoCrFeMnNi samples are displayed in Fig. 2; corresponding plots for CoCrFeNi samples are displayed in Fig. S2 in SI. As seen, the load at which the first pop-in occurs, P_I, varies widely. The deformation prior to the first pop-in during spherical indentation is purely elastic and follows the relation obtained by Hertz's contact mechanics model [30]:

$$P = \frac{4}{3} E_r R_i^{\frac{1}{2}} h^{\frac{3}{2}} \quad (1)$$

where E_r is the reduced modulus that can be determined from the Young's moduli, E, and Poisson's ratios, ν, of the specimen and indenter [33]. This relation is utilized to fit the near-identical P–h

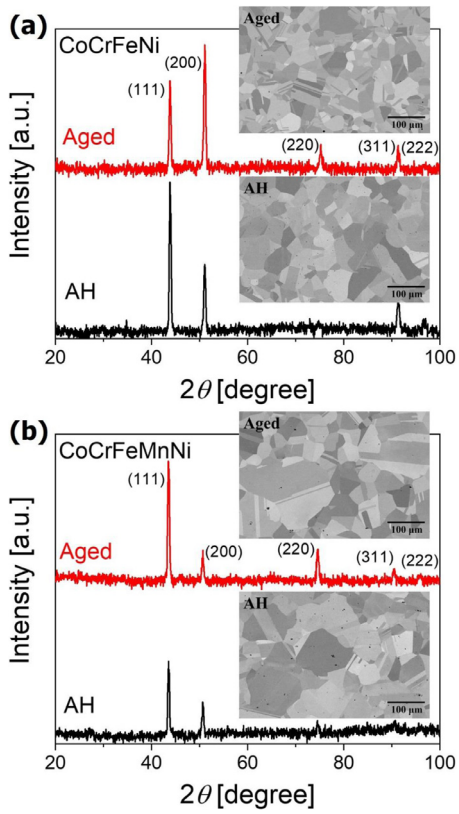

Fig. 1. The XRD patterns and BSE images of (a) CoCrFeNi and (b) CoCrFeMnNi samples.

responses before the first pop-in, so as to obtain E_r values. Using them and ν of 0.28 for CoCrFeNi and 0.26 for CoCrFeMnNi [34], E were estimated to be ~193 and ~195 GPa, respectively, which were obtained from the tests with $R_i = 12.7\ \mu$m. They, in turn, were utilized along with the measured P_l to compute the incipient shear strength (τ_y) at the first pop-in as [30]:

$$\tau_y = 0.31\left(\frac{6E_r^2}{\pi^3 R_i^2}P_l\right)^{\frac{1}{3}}. \quad (2)$$

The τ_y data obtained were plotted as a function of the cumulative probability, F, in Fig. 3. The overall ranges, mean values ($\overline{\tau_y}$), standard deviations (SD), and the coefficients of variation, CoV (defined as the ratio of the standard deviation and the mean) of $\tau_y$are listed in Table 1. The following are some observations. (i) In both the conditions, the mean values of τ_y obtained with $R_i = 0.5\ \mu$m are always much larger than those obtained with $R_i = 12.7\ \mu$m. (ii) The CoVs for all cases together range between 12 and 15%. Yet, the distributions are not similar in all cases. For example, while the τ_y data obtained with $R_i = 0.5\ \mu$m on the AH and Aged samples of CoCrFeNi HEA are nearly identical in the range of F ~0.2–0.7, the AH sample data exhibits a pronounced tail for $F \leq 0.1$. In contrast, the minimum and maximum $\tau_y$values obtained on the AH and Aged samples of CoCrFeMnNi HEA are nearly identical. However, significant divergence between then at around $F = 0.5$ can be seen. (iii) The shapes of the distributions obtained with $R_i = 12.7\ \mu$m on both the alloys are similar, especially in CoCrFeMnNi samples, where a systematic shift in τ_y values upon aging, by about 0.15 GPa, could be noticed.

The F vs. τ_y data is often utilized to estimate the activation volume, V^*, of the source for incipient plasticity using the relation [19,22,26,35,36]:

$$F = 1 - \exp\left[-\exp\left(\frac{V^*}{kT}\tau_y + \beta\right)\right] \quad (3)$$

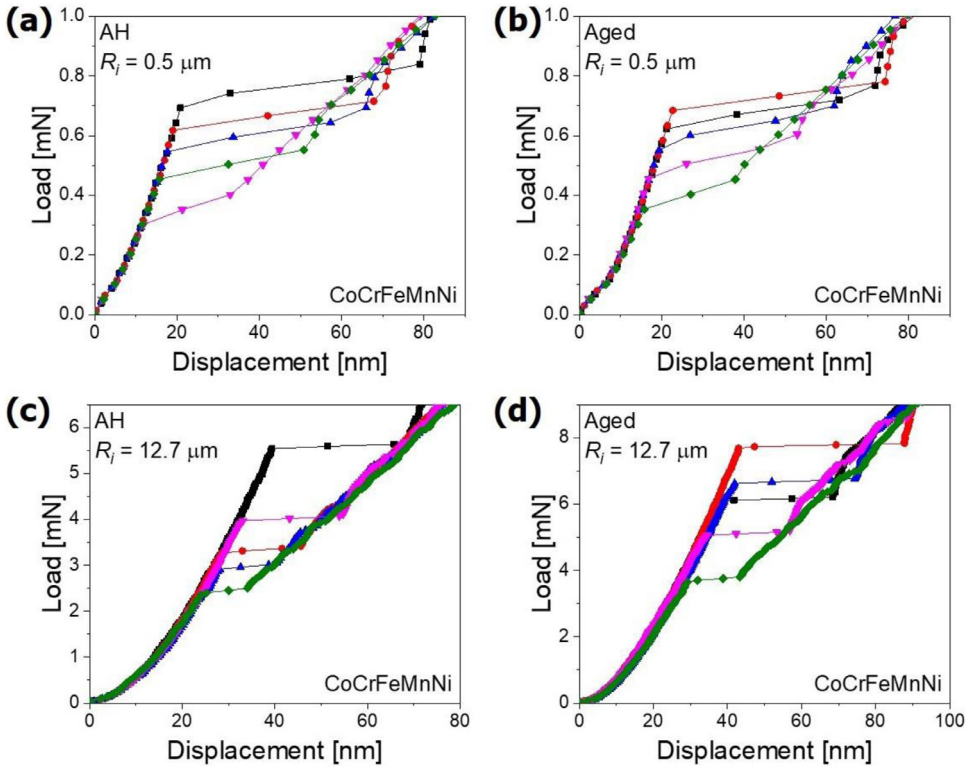

Fig. 2. Representative load-displacement curves of CoCrFeMnNi samples for the tests with $R_i = 0.5\ \mu$m [(a) and (b)] and $R_i = 12.7\ \mu$m [(c) and (d)]. (a) and (c) are for AH samples, while (b) and (d) are for Aged ones.

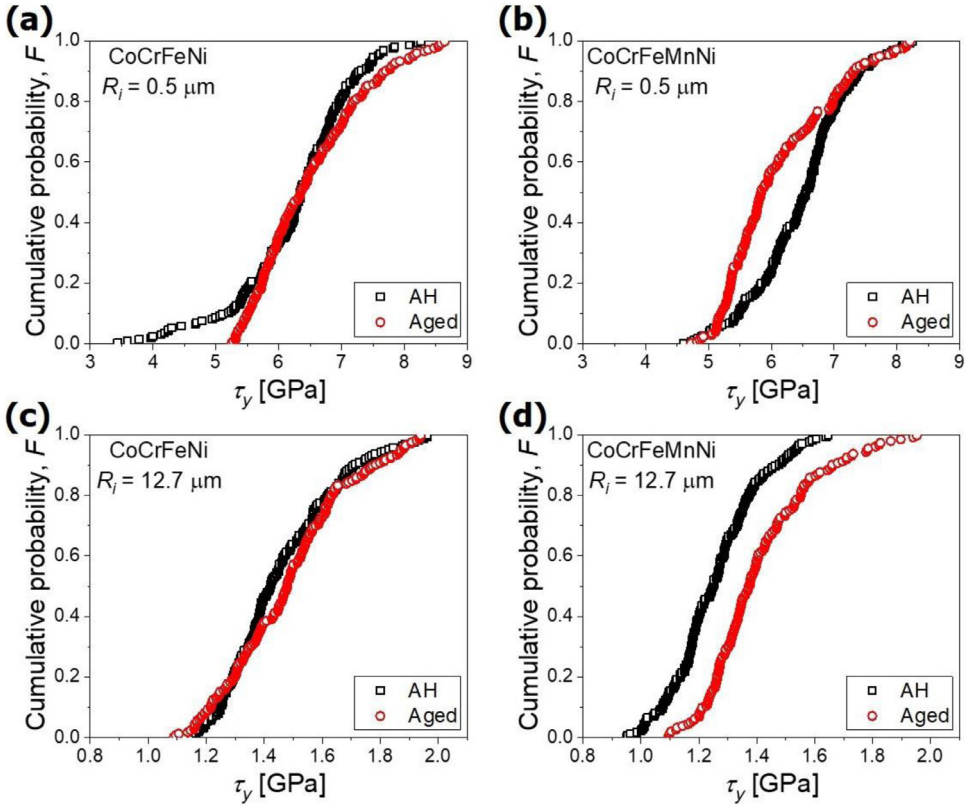

Fig. 3. Cumulative probability distributions of τ_y for the tests with R_i = 0.5 μm [(a) and (b)] and R_i = 12.7 μm [(c) and (d)]. (a) and (c) are for CoCrFeNi, while (b) and (d) are for CoCrFeMnNi.

Table 1
Summary of minimum, maximum, range, mean ($\overline{\tau_y}$), standard deviation (SD), and CoV values of $\tau_y$for each condition.

Sample		R_i [μm]	τ_y [GPa]					
			Min.	Max.	Range	$\overline{\tau_y}$	SD	CoV
CoCrFeNi	AH	0.5	3.44	8.27	4.83	6.26	0.91	15%
		12.7	1.12	1.96	0.84	1.46	0.19	13%
	Aged	0.5	5.25	8.64	3.39	6.49	0.84	13%
		12.7	1.09	1.94	0.85	1.48	0.21	14%
CoCrFeMnNi	AH	0.5	4.59	8.24	3.65	6.48	0.75	12%
		12.7	0.95	1.65	0.70	1.26	0.15	12%
	Aged	0.5	4.72	8.21	3.48	6.10	0.84	14%
		12.7	1.09	1.95	0.86	1.41	0.18	13%

where k is the Boltzmann constant, T is the absolute temperature, and β is a weak function of P_I [24,26,35]. Typically, the experimental data tends to be linear when plotted as ln[-ln(1-F)] versus τ_y, the slope of which is utilized to obtain V^* [24–26,29,36,37]. Such plots of all the data obtained in this study are displayed in Fig. S3 of SI. As seen, most of the results do not follow a single linear trend when plotted on a ln[-ln(1-F)] scale. This and the observations made in the preceding paragraph prompted us to examine the data in terms of kernel density estimates (KDEs) [20,38].

The τ_y data are displayed in Fig. 4 as KDE plots. A unimodal distribution of the probability density function (PDFs) for thermally activated, stress-assisted pop-in behavior would be a symmetric Gaussian-type distribution [18]. Clearly, this is not the case for the current results as the KDE plots show the presence of 'shoulders' in the distribution, which indicates that they may be bimodal. This, in turn, suggests that the activation of more than one deformation mechanism could be causing the elastic-to-elastoplastic transition during spherical indentation.

For the deconvolution of the PDFs, two statistical models, namely Gaussian and log-normal, were considered, to examine which one of them better describes the experimental data. The Gaussian distribution is the most widely used model for analyzing the pop-in strength statistics [11,18,39] and its PDF, f, is given as [40]:

$$f(\tau_y) = \frac{1}{\sigma\sqrt{2\pi}} \exp\left(-\frac{(\tau_y - \overline{\tau_y})^2}{2\sigma^2}\right) \quad (4)$$

where σ represents standard deviation. For the log-normal distribution model, the PDF is given as

$$f(\tau_y) = \frac{1}{\tau_y\sigma\sqrt{2\pi}} \exp\left(-\frac{(\ln\tau_y - \overline{\tau_y})^2}{2\sigma^2}\right), \ \tau_y > 0. \quad (5)$$

The intrinsic limitation of normal or Gaussian distribution is that a random variable in it can take any real value, including negative ones, whereas τ_y is always a positive quantity. The log-normal distribution does not suffer this drawback and is known to approximate multiplicative degradation processes [41,42]. Given the magnitude of a pop-in, which could involve not only the activation of a dislocation source but a subsequent rapid multiplication of such activated dislocations, log-normal distribution appears to

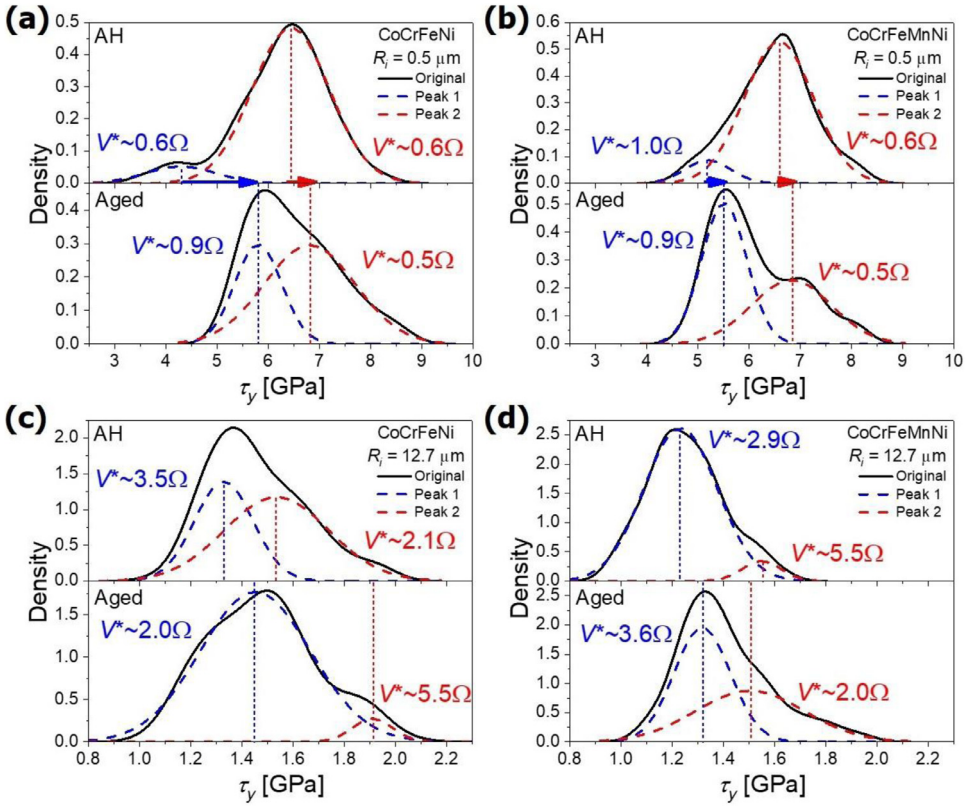

Fig. 4. The KDE curves and the deconvolution results by Gaussian distribution for the tests with R_i = 0.5 μm [(a) and (b)] and R_i = 12.7 μm [(c) and (d)]. (a) and (c) are for CoCrFeNi, while (b) and (d) are for CoCrFeMnNi. The V^* of each peak is also given in terms of Ω, and the dashed line marks the average τ_y value of each peak.

Table 2
The results of deconvolution by either Gaussian distribution or log-normal distribution and the corresponding maximum likelihood estimates (MLEs). (Deconv.: deconvoluted, LS: low strength, HS: high strength).

Sample		R_i [μm]	Deconv. peak	Gaussian distribution				Log-normal distribution			
				Proportion	$\overline{\tau_y}$	SD	Log-likelihood	Proportion	$\overline{\tau_y}$	SD	Log-likelihood
CoCrFeNi	AH	0.5	LS peak	0.09	4.29	0.68	-224.6	0.09	1.45	0.12	-225.6
			HS peak	0.91	6.44	0.75		0.91	1.86	0.11	
		12.7	LS peak	0.4	1.33	0.11	55.8	0.61	0.29	0.08	55.8
			HS peak	0.6	1.54	0.20		0.39	0.48	0.1	
	Aged	0.5	LS peak	0.34	5.80	0.46	-213.9	0.38	1.75	0.05	-212.5
			HS peak	0.66	6.81	0.89		0.62	1.93	0.11	
		12.7	LS peak	0.95	1.45	0.21	30.1	0.06	0.17	0.03	29.1
			HS peak	0.05	1.90	0.07		0.94	0.4	0.14	
CoCrFeMnNi	AH	0.5	LS peak	0.1	5.19	0.44	-221.1	0.12	1.66	0.07	-221.4
			HS peak	0.9	6.58	0.67		0.88	1.89	0.09	
		12.7	LS peak	0.94	1.23	0.14	96.8	0.94	0.21	0.11	96.9
			HS peak	0.06	1.55	0.08		0.06	0.43	0.03	
	Aged	0.5	LS peak	0.55	5.51	0.44	-205.1	0.64	1.72	0.07	-204.8
			HS peak	0.45	6.83	0.78		0.36	1.95	0.08	
		12.7	LS peak	0.54	1.32	0.11	63.8	0.8	0.29	0.09	63.9
			HS peak	0.46	1.50	0.21		0.2	0.51	0.09	

be a possible candidate. Representative plots of the deconvoluted log-normal distributions are displayed in Fig. S4 in SI.

The maximum likelihood estimates (MLEs) are utilized to assess the deconvolution results using the two distribution models (see SI for details) [20]. In general, the model that yields the highest MLE log-likelihood value for a given dataset best describes it. Results of this exercise are listed in Table 2. It can be seen from Table 2 that the log-likelihood values for the two models are nearly identical for any combination of material-experimental condition. This implies that neither of the models is superior to the others in terms of describing the data. Hence, we focus only on the deconvoluted results of the Gaussian distribution here after, given that, in general, it is the model that is most widely utilized in the published literature to describe the pop-in distributions obtained on crystalline metals thus far [11,18,39]. From Table 2, it is seen that the proportion of the high strength peak is significant (i.e., more than 10%) in five out of eight cases. While it is $\leq$ 10% in both the AH (R_i = 0.5 mm) cases and AH of CoCrFeMnNi (R_i = 12.7 mm) case, it appears reasonable to consider them also as bimodal given that the dataset sizes in all cases is very large (at about 200 points in each case).

The deconvoluted KDE plots are displayed in Fig. 4, along with the respective full (or non-deconvoluted) plots. By computing the F values for each of the deconvoluted Gaussian distribution and then

plotting ln[-ln(1-F)] versus τ_y for that particular distribution (see Figs. S5 and S6 in SI for details), V^* associated with each of the deconvoluted peak is obtained. Values of the V^* normalized with the atomic volume, Ω (= $0.25a^3$ for fcc structure) [24,36], are displayed alongside the corresponding peak in Fig. 4. The following are some observations. (i) The values of V^* obtained with R_i = 0.5 μm, which range between 0.5 and 1Ω, are much smaller than the range of 2.0 to 5.5Ω obtained with R_i = 12.7 μm. (ii) For R_i = 0.5 μm, two distinct levels of V^* occurring around ~0.5 and 1Ω could be noted. The low strength peaks, which are also the dominant ones, in the AH condition correspond to 0.6Ω; upon aging, the V^* values corresponding to the low strength peaks increase to 0.9Ω whereas the high strength peaks move to smaller V^* of 0.5 to 0.6Ω. (The only exception is that both the peaks in the CoCrFeNi sample yield a V^* ~0.5Ω). (iii) For R_i = 12.7 μm, three distinct deformation mechanisms with V^* ~2, ~3, and ~5.5 Ω appear to take place (Figs. 4c and 4d). These inferred V^* values point to the possibility that the deformation mechanisms depend on both the tip radius and the structural state of the sample, which are discussed below.

4. Discussion

4.1. Deformed volume and length scale

Before discussing the possible mechanism(s) responsible for the pop-ins, it is critical to assess the representative volume of the stressed material underneath the spherical indenter, V_s, and the length scale, d_s, associated with it. Since the deformation prior to the pop-in is elastic, the stress distribution underneath the spherical indenter should obey the Hertzian contact mechanics [30], which predicts that the maximum in the shear stress, τ_{max}, occurs at a point that is directly below the contact on the axis of symmetry, at a distance approximately half the contact radius, and decays radically outwards; see Refs. [43,44] for illustrations of this. Since τ_{max} occurs at a specific point, different authors invoked distinct assumptions to estimate V_s [26,44–47], which are briefly summarized below.

Phani et al. [45] assumed a 2D contour with a boundary where local τ_{max} is equal to the critical resolved shear stress. The area of this 2D highly stressed zone, A, is described as

$$A = \left(0.022\nu^2 - 0.0266\nu + 0.1245\right)\frac{P_l - P_\tau}{\tau_{max}} \tag{6}$$

where P_τ is the minimum load required to generate pop-in. Based on the A value, if we assume a spherical shape of the V_s (or equivalently a circular shape of area A in 2D), the diameter of the stressed volume, d_s, can thus be calculated as $\sqrt{A/\pi}$. Then spherical-shaped V_s can be calculated as $\pi d_s^3/6$.

Barnoush [44] assumed V_s to be the volume where at least 90% of peak τ_{max} value is acting. This results in a volume resembling an oblate spheroid with a major axis of $0.6a_c$ and a minor axis of $0.5a_c$, where a_c is the contact radius and can be estimated according to Hertzian model,

$$a_c = \sqrt[3]{\frac{3P_l R_i}{4E_r}} \tag{7}$$

This results in $V_s = 4\pi(0.3 \times 0.3 \times 0.25)d_s^3/3$.

Mason et al. [26] assumed that V_s scales with $(a_c)^3$ with a proportionality constant of the order ~π. The relation of $V_s \approx \pi a_c^3$ was later also applied by other researchers [24,48] to estimate the volume of the highly stressed zone and then d_s by assuming a spherical shape of V_s.

By assuming that pop-in will occur if a defect is subjected to a shear stress $\tau_{pop\text{-}in}$, Morris et al. [46] defined the volume V_s as the region where the local resolved shear stresses, τ, satisfy $\tau > \tau_{pop\text{-}in}$. The functional relationship between V_s and $\tau_{max}/\tau_{pop\text{-}in}$ is then fitted to a power law as [47]:

$$\frac{V_s}{a_c} = -2.015 \times 10^{-4}\left(\frac{\tau_{max}}{\tau_{pop-in}} - 1\right)^3 + 0.128\left(\frac{\tau_{max}}{\tau_{pop-in}} - 1\right)^2 + 5.695\left(\frac{\tau_{max}}{\tau_{pop-in}} - 1\right). \tag{8}$$

Estimated values of V_s and d_s for R_i = 0.5 μm using the aforementioned four models are listed in Table 1. Morris et al. [46] set $\tau_{pop\text{-}in}$ equal to the average τ_y for the largest indenter they have utilized in their investigation (R_i = 700 μm). Based on the reported value of $\overline{\tau_y}$(0.22 GPa) for fcc Ni obtained with an indenter having R_i = 209.4 μm [49], and that the CoCrFeNi and CoCrFeMnNi HEAs would have a solid solution strengthening effect compared to pure Ni, it is reasonable to assume a $\tau_{pop\text{-}in}$ value of approximately ~0.3 GPa. Therefore, based on the average τ_y and a_c values, V_s and d_s (by assuming a spherical shape of V_s) were obtained.

Data in Table 3 indicates that the characteristic length scale d_s ranges from ~30 to ~600 nm, depending on the model applied. The following discussion on the dislocation nucleation mechanism(s) responsible for the first pop-ins will be based on such length scale and its relationship with the density of various types of defects.

4.2. Dislocation nucleation: homogeneous vs. heterogeneous

Incipient plasticity in crystalline materials, which manifests as the pop-in during spherical indentation, may occur either by dislocation nucleation or by the slip of the pre-existing mobile dislocations. The latter can be excluded since the reported value of the critical resolved shear stress for dislocation slip in fcc HEAs (e.g. ~33–43 MPa for CoCrFeMnNi [50]) is substantially smaller than the measured τ_y. Thus, dislocation nucleation is the only possible mechanism responsible for the first pop-in. The nucleation sources can either be pre-existing dislocations themselves or vacancies; even homogeneous dislocation nucleation from defect-free lattice is a possibility although it requires a substantially large stress [18]. Based on the relative values of τ_y and V^* for each peak displayed in Fig. 4, possible dislocation nucleation mechanisms are discussed below with a focus on the results obtained with R_i = 0.5 μm first.

It has been suggested that the first pop-in during nanoindentation is associated with a homogeneous dislocation nucleation mechanism [17,51,52]. According to this hypothesis, the pop-in involves a cooperative motion of atoms to form a critical-sized dislocation loop, and, hence, the activation energy would be on the order of several eV [23,51,53,54]. From Figs. 4a and 4b, we see that the high strength peak in both the alloys in the AH condition occurs at higher τ_y and has a V^* of ~0.5Ω. The mean τ_y values of these distributions are nearly one-tenth of shear modulus G (= ~75 and 77 GPa, for CoCrFeNi and CoCrFeMnNi, respectively), and hence are close to the theoretical shear strength [49]. On this basis, we infer that this peak is likely due to the homogeneous dislocation nucleation from a defect-free zone [18,44,49]. The formation of a critical vacancy loop required for this is expected to comprise many atomic volumes, in general. However, the critical size may diminish substantially when the applied stress approaches the theoretical shear strength of the alloy [26,53]. Ngan and colleagues [55,56] have shown that a dislocation loop does not nucleate directly from the perfect crystal environment but arises out of thermal fluctuations. This, in turn, leads to the measured activation volume being in the order of the atomic sizes rather than those expected from a dislocation loop. If the dislocation density, ρ_{disl}, in each sample is taken as ~10^{12} m^{-2} that is typical in annealed metals, the mean spacing between the dislocations, l_{disl}(= $\sqrt{\rho_{disl}}$) would be ~1 μm. This is much larger than the largest possible d_s. (Recall from section 4.2 and Table 3 that the length scale d_s

Table 3
Summary of the models in literature for estimating V_s and d_s and the corresponding results applied for $R_i = 0.5$ μm of the present study.

Ref.	Parameter	CoCrFeNi		CoCrFeMnNi	
		AH	Aged	AH	Aged
Phani et al. [45]	V_s [μm^3]*	3.46×10^{-5}	2.80×10^{-5}	2.56×10^{-5}	1.75×10^{-5}
	d_s [μm]	0.0404	0.0377	0.0366	0.0322
Barnoush [44]	V_s [μm^3]$^{\perp}$	6.05×10^{-5}	6.89×10^{-5}	6.60×10^{-5}	5.62×10^{-5}
	d_s [μm]	0.0518	0.0541	0.0533	0.0505
Mason et al. [26]	V_s [μm^3] *	0.00202	0.00230	0.00220	0.00187
	d_s [μm]	0.157	0.164	0.161	0.153
Morris et al. [46]	V_s [μm^3] *	0.104	0.126	0.119	0.093
& Wu et al. [47]	d_s [μm]	0.583	0.621	0.610	0.563

* V_s is assumed to be spherical shape and d_s corresponds to the diameter for the sphere.
$^{\perp}$: V_s is assumed to be ellipsoid shape and d_s corresponds to the length of the major axis.

of highly stressed volume ranges from ~30 to ~600 nm depending on models applied). Hence, the probability of finding a pre-existing dislocation in the highly stressed volume is low and homogeneous dislocation nucleation scenario is possible in this case.

Many of the published works on pop-ins in crystalline alloys [23,24,26,57] indicate that the presence of pre-existing defects such as vacancies, vacancy clusters, dislocations, and impurities could aid in heterogeneous dislocation nucleation that leads to the pop-in. It is possible that such a mechanism is responsible for the low strength peaks observed in Figs. 4a and 4b. Indeed, the values of V^*, which are ~1.0Ω, inferred from these peaks imply that point defect like vacancies are possibly responsible for them through monovacancy-mediated dislocation nucleation [22,23,26]. To ascertain this, an estimate of the defect density is made, as following. First, let us assume that a certain type of defect is responsible for the peak observed at lower strengths. An assumption that pop-in will only occur if and only if at least one such defect exists within V_s, allows the use of the exponential (or Poisson) distribution statistics to estimate the probability for the existence of such a defect, P_{low}, within V_s [38,46] as:

$$P_{low} = 1 - \exp(-\rho_{low} V_s) \tag{9}$$

where ρ_{low} is the number density of the defects per unit volume. The ratio of the low strength peak's area to that of entire area of KDE can be taken to approximate P_{low}. From Fig. 4a and Table 2, it was estimated to be 0.09 and 0.34 for the AH and Aged CoCrFeNi samples, respectively. For $V_s = \pi a_c^3$ [24,26], these P_{low} values yield ρ_{low} as ~1.5×10^3 μm^{-3} for the AH samples and ~$0.6–1.4 \times 10^3$ μm^{-3} for Aged samples. In turn, the average spacing between the defects, $l_{low}(= \sqrt[3]{\rho_{low}})$, is estimated as ~87 and ~41–55 nm, respectively. If the vacancy concentration at thermal equilibrium at room temperature is assumed to be 10^{-6} (viz. one vacancy per million atoms) [24], the mean spacing between the vacancies, l_{vac} would be ~23 nm. The similarity in l_{low} and l_{vac} values supports the possibility of a monovacancy-mediated dislocation nucleation mechanism being responsible for the low strength peaks observed in Figs. 4a and 4b. The relatively smaller V^* for the low strength peak of AH CoCrFeNi sample (~0.5Ω instead of ~1Ω) may be due to specific feature with the vacancy size in the sample, for which further investigation will be required.

Such bimodal distribution deconvolution and the partition into homogeneous and heterogeneous dislocation nucleation is analogous to the 'master plot' for the pop-in behavior proposed by Gao et al. [18], although a different analysis protocol was applied in the current work. In their approach, Gao et al. suggested that homogeneous dislocation nucleation is favored with smaller V_S and/or lower defect density. On the other hand, heterogeneous nucleation is favored when the V_S is larger and/or the material contains higher defect density. In most cases, the collective pop-in data falls between the two asymptotes and shows a convolution response that combines both the homogeneous and heterogeneous nucleation mechanisms. Our analysis here successfully deconvolutes the two mechanisms and the respective V^* is thus available, providing insights into the plurality of possible mechanisms for the incipient plasticity.

In Table 3, he values of V^* reported in literature (wherein similar analyses of the pop-in statistics was performed) on fcc metals and alloys (including HEAs) are summarized for comparison [24–26,29,36,37]. All these studies only considered the measured distributions to be unimodal and therefore obtained only one V^* value for any given experimental condition. As seen, most report V^* to be $\leq 1\Omega$ and usually attributed it to the heterogeneous dislocation nucleation aided by preexisting dislocations, vacancies (or vacancy clusters), impurities, and/or surface asperities [22,23,26]. In contrast, Wang et al. [29] obtained $\tau_y \sim \frac{G}{7}$ and attributed it to the homogeneous dislocation nucleation, which is similar to the case of the high strength peak of the present study. To summarize, results and analyses of the data obtained on as-homogenized samples probed with a small indenter tip show that plastic deformation gets initiated at relatively lower stresses if a preexisting defect, which would aid in the onset, is present within the stressed volume. If not, homogeneous dislocation nucleation ensues at significantly higher stresses.

4.3. The effect of tip radius

The values of τ_y are considerably smaller, when a larger radius tip ($R_i = 12.7$ μm) was used, which is probably due to the indentation size effect [37,45,46,49]. With increasing R_i, a substantially larger volume of the material is probed, which, in turn, leads to an increased probability of encountering the pre-existing defects activating plasticity at a lower stress level. The relatively low τ_y values ($\sim \frac{G}{62} - \frac{G}{40}$) [49] as well as the more complicated configurations of the deconvoluted KDE curves (compared to the cases with $R_i = 0.5$ μm) suggest heterogeneous dislocation nucleation mechanism that involves cooperative motion of multiple atoms being responsible for the observed pop-ins.

From Figs. 4c and 4d and slao summarized in Table 4, we note that both the deconvoluted distributions in each KDE plot yield relatively large V^* values (~2.0–5.5Ω), as compared to those obtained with $R_i = 0.5$ μm. In all, three types of distinct V^* values can be noted. Category I has V^* ~2.0Ω and the peak in τ_y occurring at ~1.5 GPa with a relatively broad distribution. The high strength peaks in AH CoCrFeNi and Aged CoCrFeMnNi, and the low strength peak in Aged CoCrFeNi belong to this category. Category II has V^* ranging between 2.9 and 3.6 Ω with τ_y peaking at ~1.3 GPa with a relatively narrower distribution, as seen in the low strength peaks of AH CoCrFeNi and both AG and Aged CoCrFeMnNi samples. The third and final category III has V^* ~5.5Ω with τ_y ranging between ~1.6 or 1.9 GPa with a very shallow and narrow distribution,

Table 4
Summary of literature on the V^* obtained by applying pop-in statistical analysis and the corresponding dislocation nucleation mechanism of fcc metals and alloys.

Material	Tip radius [μm]	V^*/Ω	Mechanism	Dislocation nucleation site	Ref.
CoCrFeNi & CoCrFeMnNi	0.5	~0.5	Homogeneous	--	This study
		~1.0	Heterogeneous	Monovacancy	
	12.7	~2.0		Vacancy cluster	
		~2.9–3.5		Dislocation	
		~5.5		Grain boundary	
sc-Ni	0.22	1	Homogeneous	--	[29]
sc-Ni	0.1	0.4–0.6	Heterogeneous	Dislocation	[37]
	1	0.4–0.6			
	1.3	0.1–0.3			
Ni	unknown	0.3		Dislocation, vacancy (cluster),	[25]
sc-Pt	0.15	0.7		impurity, or surface asperity	[26]
CoCrNi	unknown	0.4	Heterogeneous	Dislocation, vacancy (cluster),	[25]
Al0.1CoCrFeNi		0.7		impurity, or surface asperity	
CoCrFeMnNi		0.8			
CoCrFeMnNi	8.08	2–4		Vacancy (cluster)	[36]
sc-CoCrFeMnNi	0.638	3			[24]

seen in the Aged CoCrFeNi and AH CoCrFeMnNi samples. While it may not be possible to precisely identify the micromechanisms responsible for each of these categories of distributions, due to large V_S that could potentially interact with a number of different microstructural features such as grain boundaries, an attempt is made below to identify them in an approximate manner.

First, we assume that two distinct sets of defects are responsible for the two deconvoluted peaks in each case, i.e. a 'low-stress defect' for the low strength peak and a 'high-stress defect' for the second (high strength) one. Since the category II peaks are of lower strength, we use Eq. (9) to estimate the defect density associated with it. If a pop-in is assumed to occur if and only if at least one 'low-stress' defect exists within V_s, Eq. (9) can be used to estimate P_{low}. (It is important to recognize here that this argument will hold true only for the low-stress defect as it would be the first one to get triggered even if there are high-stress defects present in V_s.) For $V_s \approx \pi a_c^3$ [24,26], the estimated P_{low} values result in ρ_{low} ranging between ~1.0 and 8.5 μm^{-3} and l_{low} between ~0.5–1.0 μm, which is similar to l_{disl} of 1 μm in well-annealed metals. This similarity suggests that pre-existing dislocations are possibly the low-stress defects responsible for the category II peaks in Figs. 4c and 4d.

Turning to category III peaks, we note from Table 2 that both constitute relatively small proportions (5% in the case of Aged CoCrFeNi and 6% in the CoCrFeMnNi) in the overall distributions. The large value V^* (~5.5Ω) points to the possibility of dislocation nucleation from gran boundaries being the mechanism responsible as it involves a relatively large number of atoms. Both these observations suggest that these peaks are probably a result of the indentions made either on grain boundaries or sufficiently close to them such that they become active. This relatively large size of the indenter tip increases such encounters becoming reasonably significant. For category I, prior studies on CoCrFeMnNi HEA [24,36] that reported V^* in the range of ~2–4Ω, suggested that vacancy or vacancy cluster mediated heterogeneous dislocation nucleation involving several atoms as being responsible for this.

To summarize the results obtained with the larger indenter, it is quite clear that plastic deformation gets initiated at relatively low stresses when the stressed volume contains pre-existing dislocations. If not, heterogeneous dislocations nucleation aided either by vacancies or grain boundaries would occur at higher indentation loads. Further studies on specific microstructural feature, for instance single crystal HEA with and without pre-strain (for critically examining the role of preexisting dislocation density), when using relatively large spherical tip may be required for further elucidation of these mechanisms.

4.4. Aging effect on dislocation nucleation

From Figs. 4a and 4b, we note that both the low strength and high strength peaks move to higher stress values upon aging; the values of V^* for the respective peaks do not change, however. While the high strength peaks dominate both the KDE plots of the AH samples, the low strength peaks are more dominant in the Aged samples. These two observations provide clues for the influence of the SRO domains, whose degree is expected to be enhanced by thermal aging followed by slow furnace cooling [11,58], on the incipient plasticity of HEAs examined. It is widely reported that SROs affect both the nucleation and subsequent mobility of dislocations in HEAs in a significant manner by elevating the overall lattice friction resistance to dislocation motion, thus contributing to the solid solution strengthening of HEAs [13,14,58–60]. Recent studies that employed molecular dynamics (MD) simulations [61,62] suggest that short range ordering makes the dislocation nucleation difficult and hence increases the yield strength of the HEA. Complementary calculations using density functional theory [61] reveal that a localized electronic structure of Cr atoms in the CoCrNi alloy, which weakens the Cr-Cr bonding in a local chemical ordering process, and, in turn, facilitates the formation of nanoscale bcc-like defects. It was hypothesized that such defects act as precursors for the homogeneous dislocation nucleation.

Using energy-filtered transmission electron microscopy, Zhang et al. [11] estimated that the average SRO domain has a size of 1.13 ± 0.43 nm in a CoCrNi alloy. Assuming it to be spherical in shape, its volume would be ~0.76 nm^3 or ~70Ω. If the SRO domains in all CoCrNi-based HEAs are assumed to be similar in size, the estimated SRO domain size is too large to be the nucleation site for a single dislocation. Instead, an overall strengthening effect induced by SRO, as the increase in τ_y values upon aging seen in Figs. 4a and 4b, is more likely. This scenario is consistent with the MD simulation results [62] that increasing degree of SRO induces higher SFE and thus increased difficulty in emitting dislocations when the unstable SFE of the surrounding regions is higher. Additional support for this hypothesis can be obtained from the full width at half maximum (FWHM) of the high strength peaks, which increase from ~1.78 to ~2.23 GPa in CoCrFeNi and from ~1.59 to ~1.85 GPa in CoCrFeMnNi upon aging as shown in Figs. 5a and 5b, respectively. Since the SRO domains widen the energy landscape spectrum of the atomic structure, an enhancement in FWHM upon aging due either to increased number of SRO domains or coarsening of the domains that are already present in the AH state of the alloy, could be expected. MD simulations by Ma and colleagues [13,14] showed that the distribution in the SFEs, which is sensitive to local chem-

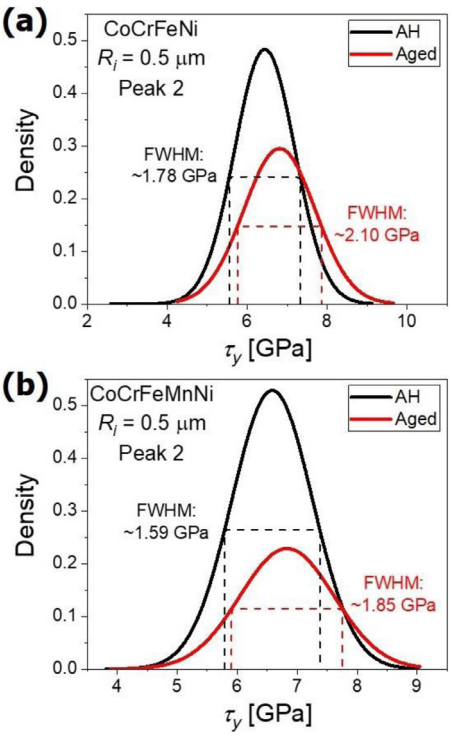

Fig. 5. Comparison of the FWHM of the high strength peak for the tests with $R_i = 0.5\ \mu$m in (a) CoCrFeNi and (b) CoCrFeMnNi HEAs.

ical configuration, in a CoCrNi alloy becomes asymmetric and has higher FWHM when a larger fraction of SRO is present in the microstructure. Since the high strength peaks in Figs. 4a and 4b originate from homogeneous dislocation nucleation (from a defect-free lattice), the FWHM of their τ_y distributions would also increase with enhanced degree of SRO due to a wider distribution in the energy landscape compared to a random solid solution, which is exactly what is observed here as shown in Fig. 5. In the Aged condition, the increased energy barrier for the dislocation nucleation due to the increased SRO content may be the reason for the reduced intensity of the high strength peak that corresponds to homogeneous dislocation nucleation.

Before closing, a commentary on the inference of the above observations to the overall microscopic structural nature of HEAs and their macroscopic plastic deformation would be instructive. The results of this study unambiguously demonstrate that the dominant deformation mechanism inferred from the statistical analyses depends on the length scale at which the material's response is probed as well as on the condition the alloy is in. Importantly, the results also show that alternative mechanisms are available for accommodating the applied stress through plastic flow for any given combination of alloy condition-probed length scale. While it is likely that any metallic alloy—whether it is a HEA or not—would also have several mechanistic possibilities on its palette, the uniqueness of HEAs is perhaps the fact that the strength distributions associated with these disparate mechanisms overlap, i.e., they are not widely separated as in conventional alloy contexts. The latter point is amply exemplified by the bimodality in almost all the pop-in strength data distributions examined in the present work. In the case of dilute alloys or pure elements, only plastic deformation mechanisms that can be activated at lower stresses will get sampled, because the others would require far too higher stresses. The plurality of available mechanisms affirms the fact that HEAs—even the best amongst them in terms of monophasic nature—are heterogeneous at the nanoscopic length scales. This, plus the high concentration of alloying elements in them (and hence the distorted lattices), render near-simultaneous activation of different mechanisms depending on imposed deformation parameters such as temperature, strain, and strain rate, on the HEA a possibility. Hence, it is entirely likely that some of the unique features of HEAs—in terms of their strength-ductility-toughness combinations—are due to this intrinsic ability of them to trigger different mechanism as the experimental situation demands.

5. Summary

Nanoindentation tests with spherical tips were performed on two equiatomic CoCrFeNi and CoCrFeMnNi HEAs with fcc crystal structures to examine the stochastic nature of the incipient plasticity in them, and in turn, infer the micromechanisms responsible for elastic-to-elastoplastic deformation. Statistical analyses of the distribution in strengths that correspond to the first pop-in loads clearly indicates that they are bimodal in nature. The deconvoluted distributions were analyzed to estimate the activation volumes of the underlying deformation processes. When the volume of the material probed is small (by using a spherical tip with $R_i = 0.5\ \mu$m), the onset of plastic deformation is aided by heterogeneous dislocation nucleation if the probed volume contains monovacancies; if not, homogeneous dislocation nucleation causes incipient plasticity at higher stresses. When the probed volume is considerably large (through the use of a larger indenter with $R_i = 12.7\ \mu$m), in addition to an overall strength reduction due to the spherical indentation size effect, the deformation mechanisms switch over to preexisting dislocation mediated one at low stresses and vacancy cluster or grain boundary aided heterogeneous dislocations nucleation at higher stresses. An increase in the chemical short range order, via a high temperature aging, strengthens the alloys by enhancing the stress required for homogeneous dislocation nucleation.

Declaration of Competing Interest

The authors declare that they have no known competing financial interests or personal relationships that could have appeared to influence the work reported in this paper.

Acknowledgements

We thank Dr. Jin-Yoo Suh of Korea Institute of Science and Technology for providing the specimens and Shankha Nag of École polytechnique fédérale de Lausanne for the discussion on statistical analysis. The work at Nanyang Technological University was supported by the funding from A*STAR via the Structural Metals and Alloys Programme (No. A18B1b0061). The work at Hanyang University was supported by the National Research Foundation of Korea (NRF) grants funded by the Korea government (MSIT) (No. 2020R1A2B5B01001446 and No. 2020R1A5A6017701).

Supplementary materials

Supplementary material associated with this article can be found, in the online version, at doi:10.1016/j.actamat.2020.10.066.

References

[1] B. Cantor, I.T.H. Chang, P. Knight, A.J.B. Vincent, Microstructural development in equiatomic multicomponent alloys, Mater. Sci. Eng. A. 375–377 (2004) 213–218, doi:10.1016/j.msea.2003.10.257.
[2] D.B. Miracle, O.N. Senkov, A critical review of high entropy alloys and related concepts, Acta Mater 122 (2017) 448–511, doi:10.1016/j.actamat.2016.08.081.
[3] Z. Li, S. Zhao, R.O. Ritchie, M.A. Meyers, Mechanical properties of high-entropy alloys with emphasis on face-centered cubic alloys, Prog. Mater. Sci. 102 (2019) 296–345, doi:10.1016/j.pmatsci.2018.12.003.

[4] Y. Zhao, D.-H. Lee, M.-Y. Seok, J.-A. Lee, M.P. Phaniraj, J.-Y. Suh, H.-Y. Ha, J.-Y. Kim, U. Ramamurty, J. Jang, Resistance of CoCrFeMnNi high-entropy alloy to gaseous hydrogen embrittlement, Scr. Mater. 135 (2017) 54–58, doi:10.1016/j.scriptamat.2017.03.029.

[5] Y. Zhao, X. Wang, T. Cao, J.K. Han, M. Kawasaki, J. il Jang, H.N. Han, U. Ramamurty, L. Wang, Y. Xue, Effect of grain size on the strain rate sensitivity of CoCrFeNi high-entropy alloy, Mater. Sci. Eng. A. 782 (2020) 139281, doi:10.1016/j.msea.2020.139281.

[6] T.M. Smith, M.S. Hooshmand, B.D. Esser, F. Otto, D.W. Mccomb, E.P. George, M. Ghazisaeidi, M.J. Mills, Atomic-scale characterization and modeling of 60°dislocations in a high-entropy alloy, Acta Mater 110 (2016) 352–363, doi:10.1016/j.actamat.2016.03.045.

[7] X.D. Xu, P. Liu, Z. Tang, A. Hirata, S.X. Song, T.G. Nieh, P.K. Liaw, C.T. Liu, M.W. Chen, Transmission electron microscopy characterization of dislocation structure in a face-centered cubic high-entropy alloy Al0.1CoCrFeNi, Acta Mater 144 (2018) 107–115, doi:10.1016/j.actamat.2017.10.050.

[8] J. Ding, Q. Yu, M. Asta, R.O. Ritchie, Tunable stacking fault energies by tailoring local chemical order in CrCoNi medium-entropy alloys, Proc. Natl. Acad. Sci. 115 (2018) 8919–8924, doi:10.1073/pnas.1808660115.

[9] C. Niu, A.J. Zaddach, A.A. Oni, X. Sang, J.W. Hurt, J.M. LeBeau, C.C. Koch, D.L. Irving, Spin-driven ordering of Cr in the equiatomic high entropy alloy NiFeCrCo, Appl. Phys. Lett. 106 (2015) 161906, doi:10.1063/1.4918996.

[10] F.X. Zhang, S. Zhao, K. Jin, H. Xue, G. Velisa, H. Bei, R. Huang, J.Y.P. Ko, D.C. Pagan, J.C. Neuefeind, W.J. Weber, Y. Zhang, Local Structure and Short-Range Order in a NiCoCr Solid Solution Alloy, Phys. Rev. Lett. 118 (2017) 205501, doi:10.1103/PhysRevLett.118.205501.

[11] R. Zhang, S. Zhao, J. Ding, Y. Chong, T. Jia, C. Ophus, M. Asta, R.O. Ritchie, A.M. Minor, Short-range order and its impact on the CrCoNi medium-entropy alloy, Nature 581 (2020) 283–287, doi:10.1038/s41586-020-2275-z.

[12] A. Tamm, A. Aabloo, M. Klintenberg, M. Stocks, A. Caro, Atomic-scale properties of Ni-based FCC ternary, and quaternary alloys, Acta Mater 99 (2015) 307–312, doi:10.1016/j.actamat.2015.08.015.

[13] Q.J. Li, H. Sheng, E. Ma, Strengthening in multi-principal element alloys with local-chemical-order roughened dislocation pathways, Nat. Commun. 10 (2019) 1–11, doi:10.1038/s41467-019-11464-7.

[14] E. Ma, Unusual dislocation behavior in high-entropy alloys, Scr. Mater. 181 (2020) 127–133, doi:10.1016/j.scriptamat.2020.02.021.

[15] S.I. Hong, J. Moon, S.K. Hong, H.S. Kim, Thermally activated deformation and the rate controlling mechanism in CoCrFeMnNi high entropy alloy, Mater. Sci. Eng. A. 682 (2017) 569–576, doi:10.1016/j.msea.2016.11.078.

[16] T.F. Page, W.C. Oliver, C.J. McHargue, The deformation behavior of ceramic crystals subjected to very low load (nano)indentations, J. Mater. Res. 7 (1992) 450–473, doi:10.1557/JMR.1992.0450.

[17] H. Bei, Y.F. Gao, S. Shim, E.P. George, G.M. Pharr, Strength differences arising from homogeneous versus heterogeneous dislocation nucleation, Phys. Rev. B - Condens. Matter Mater. Phys. 77 (2008) 2–5, doi:10.1103/PhysRevB.77.060103.

[18] Y. Gao, H. Bei, Strength statistics of single crystals and metallic glasses under small stressed volumes, Prog. Mater. Sci. 82 (2016) 118–150, doi:10.1016/j.pmatsci.2016.05.002.

[19] Y. Zhao, I.C. Choi, M.Y. Seok, M.H. Kim, D.H. Kim, U. Ramamurty, J.Y. Suh, J. Il Jang, Effect of hydrogen on the yielding behavior and shear transformation zone volume in metallic glass ribbons, Acta Mater 78 (2014) 213–221, doi:10.1016/j.actamat.2014.06.046.

[20] S. Nag, R.L. Narayan, J. Jang, C. Mukhopadhyay, U. Ramamurty, Statistical nature of the incipient plasticity in amorphous alloys, Scr. Mater. 187 (2020) 360–365, doi:10.1016/j.scriptamat.2020.06.045.

[21] A.H.W. Ngan, L. Zuo, P.C. Wo, Size dependence and stochastic nature of yield strength of micron-sized crystals: A case study on Ni3Al, Proc. R. Soc. A Math. Phys. Eng. Sci. 462 (2006) 1661–1681, doi:10.1098/rspa.2005.1645.

[22] C.A. Schuh, A.C. Lund, Application of nucleation theory to the rate dependence of incipient plasticity during nanoindentation, J. Mater. Res. 19 (2004) 2152–2158, doi:10.1557/JMR.2004.0276.

[23] C.A. Schuh, J.K. Mason, A.C. Lund, Quantitative insight into dislocation nucleation from high-temperature nanoindentation experiments, Nat. Mater. 4 (2005) 617–621, doi:10.1038/nmat1429.

[24] C. Zhu, Z.P. Lu, T.G. Nieh, Incipient plasticity and dislocation nucleation of FeCoCrNiMn high-entropy alloy, Acta Mater 61 (2013) 2993–3001, doi:10.1016/j.actamat.2013.01.059.

[25] S. Mridha, M. Sadeghilaridjani, S. Mukherjee, Activation volume and energy for dislocation nucleation in multi-principal element alloys, Metals (Basel) 9 (2019) 27–33, doi:10.3390/met9020263.

[26] J.K. Mason, A.C. Lund, C.A. Schuh, Determining the activation energy and volume for the onset of plasticity during nanoindentation, Phys. Rev. B - Condens. Matter Mater. Phys. 73 (2006) 1–14, doi:10.1103/PhysRevB.73.054102.

[27] J.H. Perepezko, S.D. Imhoff, M.-W. Chen, J. Wang, S. Gonzalez, Nucleation of shear bands in amorphous alloys, Proc. Natl. Acad. Sci. U. S. A. 111 (2014) 3938–3942, doi:10.1073/pnas.1321518111.

[28] D.E. Kramer, K.B. Yoder, W.W. Gerberich, Surface constrained plasticity: Oxide rupture and the yield point process, Philos. Mag. A Phys. Condens. Matter, Struct. Defects Mech. Prop. 81 (2001) 2033–2058, doi:10.1080/01418610108216651.

[29] L. Wang, H. Bei, T.L. Li, Y.F. Gao, E.P. George, T.G. Nieh, Determining the activation energies and slip systems for dislocation nucleation in body-centered cubic Mo and face-centered cubic Ni single crystals, Scr. Mater. 65 (2011) 179–182, doi:10.1016/j.scriptamat.2011.03.036.

[30] K.L. Johnson, Contact Mechanics, Cambridge University Press, 1985, doi:10.1017/CBO9781139171731.

[31] W.H. Liu, Y. Wu, J.Y. He, T.G. Nieh, Z.P. Lu, Grain growth and the Hall-Petch relationship in a high-entropy FeCrNiCoMn alloy, Scr. Mater. 68 (2013) 526–529, doi:10.1016/j.scriptamat.2012.12.002.

[32] Z. Wang, Q. Wu, W. Zhou, F. He, C. Yu, D. Lin, J. Wang, C.T. Liu, Quantitative determination of the lattice constant in high entropy alloys, Scr. Mater. 162 (2019) 468–471, doi:10.1016/j.scriptamat.2018.12.022.

[33] W.C. Oliver, G.M. Pharr, An improved technique for determining hardness and elastic modulus using load and displacement sensing indentation experiments, J. Mater. Res. 7 (1992) 1564–1583, doi:10.1557/JMR.1992.1564.

[34] Z. Wu, H. Bei, G.M. Pharr, E.P. George, Temperature dependence of the mechanical properties of equiatomic solid solution alloys with face-centered cubic crystal structures, Acta Mater 81 (2014) 428–441, doi:10.1016/j.actamat.2014.08.026.

[35] Y.X. Ye, Z.P. Lu, T.G. Nieh, Dislocation nucleation during nanoindentation in a body-centered cubic TiZrHfNb high-entropy alloy, Scr. Mater. 130 (2017) 64–68, doi:10.1016/j.scriptamat.2016.11.019.

[36] G. Yang, Y. Zhao, D.-H. Lee, J.-M. Park, M.-Y. Seok, J.-Y. Suh, U. Ramamurty, J. Jang, Influence of hydrogen on incipient plasticity in CoCrFeMnNi high-entropy alloy, Scr. Mater. 161 (2019) 23–27, doi:10.1016/j.scriptamat.2018.10.010.

[37] S.K. Lawrence, D.F. Bahr, H.M. Zbib, Crystallographic orientation and indenter radius effects on the onset of plasticity during nanoindentation, J. Mater. Res. 27 (2012) 3058–3065, doi:10.1557/jmr.2012.368.

[38] J.H. Perepezko, S.D. Imhoff, M.W. Chen, J.Q. Wang, S. Gonzalez, Nucleation of shear bands in amorphous alloys, Proc. Natl. Acad. Sci. U. S. A. 111 (2014) 3938–3942, doi:10.1073/pnas.1321518111.

[39] T.L. Li, Y.F. Gao, H. Bei, E.P. George, Indentation Schmid factor and orientation dependence of nanoindentation pop-in behavior of NiAl single crystals, J. Mech. Phys. Solids. 59 (2011) 1147–1162, doi:10.1016/j.jmps.2011.04.003.

[40] R.V. Hogg, J.W. McKean, A.T Allen, T. Craig, Introduction to mathematical statistics, Pearson, 2013.

[41] P.A. Tobias, D. Trindade, Applied Reliability, Third Edition, Taylor & Francis, 2011.

[42] J. Sutton, Gibrat's Legacy, J. Econ. Lit. 35 (1997) 40–59.

[43] H. Bei, Z.P. Lu, E.P. George, Theoretical Strength and the Onset of Plasticity in Bulk Metallic Glasses Investigated by Nanoindentation with a Spherical Indenter, Phys. Rev. Lett. 93 (2004) 125504, doi:10.1103/PhysRevLett.93.125504.

[44] A. Barnoush, Correlation between dislocation density and nanomechanical response during nanoindentation, Acta Mater 60 (2012) 1268–1277, doi:10.1016/j.actamat.2011.11.034.

[45] P. Sudharshan Phani, K.E. Johanns, E.P. George, G.M. Pharr, A stochastic model for the size dependence of spherical indentation pop-in, J. Mater. Res. 28 (2013) 2728–2739, doi:10.1557/jmr.2013.254.

[46] J.R. Morris, H. Bei, G.M. Pharr, E.P. George, Size Effects and Stochastic Behavior of Nanoindentation Pop In, Phys. Rev. Lett. 106 (2011) 165502, doi:10.1103/PhysRevLett.106.165502.

[47] D. Wu, J.R. Morris, T.G. Nieh, Effect of tip radius on the incipient plasticity of chromium studied by nanoindentation, Scr. Mater. 94 (2015) 52–55, doi:10.1016/j.scriptamat.2014.09.017.

[48] D. Wu, T.G. Nieh, Incipient plasticity and dislocation nucleation in body-centered cubic chromium, Mater. Sci. Eng. A 609 (2014) 110–115, doi:10.1016/j.msea.2014.04.107.

[49] S. Shim, H. Bei, E.P. George, G.M. Pharr, A different type of indentation size effect, Scr. Mater. 59 (2008) 1095–1098, doi:10.1016/j.scriptamat.2008.07.026.

[50] N.L. Okamoto, S. Fujimoto, Y. Kambara, M. Kawamura, Z.M.T. Chen, H. Matsunoshita, K. Tanaka, H. Inui, E.P. George, Size effect, critical resolved shear stress, stacking fault energy, and solid solution strengthening in the CrMnFeCoNi high-entropy alloy, Sci. Rep. 6 (2016) 1–10, doi:10.1038/srep35863.

[51] Y.L. Chiu, A.H.W. Ngan, Time-dependent characteristics of incipient plasticity in nanoindentation of a Ni3Al single crystal, Acta Mater 50 (2002) 1599–1611, doi:10.1016/S1359-6454(02)00025-3.

[52] D. Lorenz, A. Zeckzer, U. Hilpert, P. Grau, H. Johansen, H.S. Leipner, Pop-in effect as homogeneous nucleation of dislocations during nanoindentation, Phys. Rev. B - Condens. Matter Mater. Phys. 67 (2003) 1–4, doi:10.1103/PhysRevB.67.172101.

[53] G. Xu, A.S. Argon, Homogeneous nucleation of dislocation loops under stress in perfect crystals, Philos. Mag. Lett. 80 (2000) 605–611, doi:10.1080/09500830050134318.

[54] T.A. Michalske, J.E. Houston, Dislocation nucleation at nano-scale mechanical contacts, Acta Mater 46 (1998) 391–396, doi:10.1016/S1359-6454(97)00270-X.

[55] L. Zuo, A.H.W. Ngan, G.P. Zheng, Size dependence of incipient dislocation plasticity in Ni3Al, Phys. Rev. Lett. 94 (2005) 1–4, doi:10.1103/PhysRevLett.94.095501.

[56] P.C. Wo, L. Zuo, A.H.W. Ngan, Time-dependent incipient plasticity in Ni3Al as observed in nanoindentation, J. Mater. Res. 20 (2005) 489–495, doi:10.1557/JMR.2005.0056.

[57] I. Salehinia, D.F. Bahr, The impact of a variety of point defects on the inception of plastic deformation in dislocation-free metals, Scr. Mater. 66 (2012) 339–342, doi:10.1016/j.scriptamat.2011.11.028.

[58] Y. Wu, F. Zhang, X. Yuan, H. Huang, X. Wen, Y. Wang, M. Zhang, H. Wu, X. Liu, H. Wang, S. Jiang, Z. Lu, Short-range ordering and its effects on mechanical properties of high-entropy alloys, J, Mater. Sci. Technol. 62 (2021) 214–220, doi:10.1016/j.jmst.2020.06.018.

[59] Q. Ding, Y. Zhang, X. Chen, X. Fu, D. Chen, S. Chen, L. Gu, F. Wei, H. Bei, Y. Gao, M. Wen, J. Li, Z. Zhang, T. Zhu, R.O. Ritchie, Q. Yu, Tuning element distribution, structure and properties by composition in high-entropy alloys, Nature 574 (2019) 223–227, doi:10.1038/s41586-019-1617-1.
[60] E. Antillon, C. Woodward, S.I. Rao, B. Akdim, T.A. Parthasarathy, Chemical short range order strengthening in a model FCC high entropy alloy, Acta Mater 190 (2020) 29–42, doi:10.1016/j.actamat.2020.02.041.
[61] F.-H. Cao, Y.-J. Wang, L.-H. Dai, Novel atomic-scale mechanism of incipient plasticity in a chemically complex CrCoNi medium-entropy alloy associated with inhomogeneity in local chemical environment, Acta Mater 194 (2020) 283–294, doi:10.1016/j.actamat.2020.05.042.
[62] W.-R. Jian, Z. Xie, S. Xu, Y. Su, X. Yao, I.J. Beyerlein, Effects of lattice distortion and chemical short-range order on the mechanisms of deformation in medium entropy alloy CoCrNi, Acta Mater 199 (2020) 352–369, doi:10.1016/j.actamat.2020.08.044.